



Cite this: *Soft Matter*, 2022, 18, 2910

Received 10th December 2021,
Accepted 8th March 2022

DOI: 10.1039/d1sm01761f

rsc.li/soft-matter-journal

Edible mechanical metamaterials with designed fracture for mouthfeel control

André Souto,^a Jian Zhang,^{ib} Alejandro M. Aragón,^{ib}*^b Krassimir P. Velikov^{ib}*^{acd} and Corentin Coulais^{ib}*^a

Metamaterials can display unusual and superior properties that come from their carefully designed structure rather than their composition. Metamaterials have permeated large swathes of science, including electromagnetics and mechanics. Although metamaterials hold the promise for realizing technological advances, their potential to enhance interactions between humans and materials has largely remained unexplored. Here, we devise a class edible mechanical metamaterials with tailored fracture properties to control mouthfeel sensory experience. Using chocolate as a model material, we first demonstrate how to create and control the fracture anisotropy, and the number of cracks, and demonstrate that these properties are captured in mouthfeel experience. We further use topology optimization to rationally design edible metamaterials with maximally anisotropic fracture strength. Our work opens avenues for the use of metamaterials to control fracture and to enhance human-matter interactions.

fracture could be used to enhance interactions between humans and materials. In particular, little is known about how to use tunable fracture to control mouthfeel and sensory experience upon biting.¹¹ Controlling sensory experience is an important topic for the design of food products such as soups,¹² yogurts,¹³ crackers,¹⁴ cookies,¹⁵ insects,¹⁶ as well as emulsions¹⁷ and protein-based¹⁷ food products. Although the role of mechanical contrast is generally recognized to influence mouthfeel¹⁸ and the use of 3d printing is emerging as a promising avenue to shape the texture of food products,¹⁹ the use of mechanical metamaterials for tunable mouthfeel has not been explored.

Here we demonstrate that suitably designed edible mechanical metamaterial with controllable fracture properties also have tunable mouthfeel. Namely, we use anisotropic structures to control the ease of bite and use spiral-shaped structures to control the perceived number of cracks. We further demonstrate that topology optimization allows the design of structures with anisotropic fracture properties. Our findings open avenues for design of mouthfeel using edible metamaterials and the topological design of fracture properties.

Introduction

Mechanical metamaterials are man-made structures whose architecture provides unique and tunable properties.^{1–3} In particular, mechanical metamaterials have shown a wide variety of properties, from enhanced strength-to-weight ratio⁴ and dissipation,⁵ to programmable mechanical⁶ and shape-changing properties.⁷ A particularly interesting avenue for mechanical metamaterials is the design of tunable fracture and strength properties.^{4,8–10}

Tunable fracture properties have tantalizing prospects for engineering applications where strong and tough structures are much needed. However, little is known about how designed

Results

Design of mouthfeel anisotropy

We start by a range of S-shaped mechanical metamaterials shown in Fig. 1b, which we test both mechanically (Fig. 1a) as well as with a sensory assessment (Fig. 1c). In the present study, we restrict our attention to chocolate as a model brittle material and we use 3D printing to prototype the desired architectures—see Methods for details on the design approach, the 3D printing, and the mechanical testing protocols. First, the mechanical compression tests reveal that each mechanical metamaterial has a very different fracture behavior depending on whether it is compressed along one axis or the other. When the structure is compressed along its horizontal direction, the structure is relatively stiff, strong, of comparable stiffness and strength to

^a Institute of Physics, University of Amsterdam, 1098 XH Amsterdam, The Netherlands. E-mail: Krassimir.Velikov@unilever.com, coulais@uva.nl

^b Faculty of Mechanical, Maritime and Materials Engineering, Delft University of Technology, Mekelweg 2, 2628 CD Delft, The Netherlands. E-mail: a.m.aragon@tudelft.nl

^c Unilever Innovation Centre Wageningen, 6708 WH Wageningen, The Netherlands

^d Debye Institute for NanoMaterials Science, Utrecht University, 3584 CC, Utrecht, The Netherlands



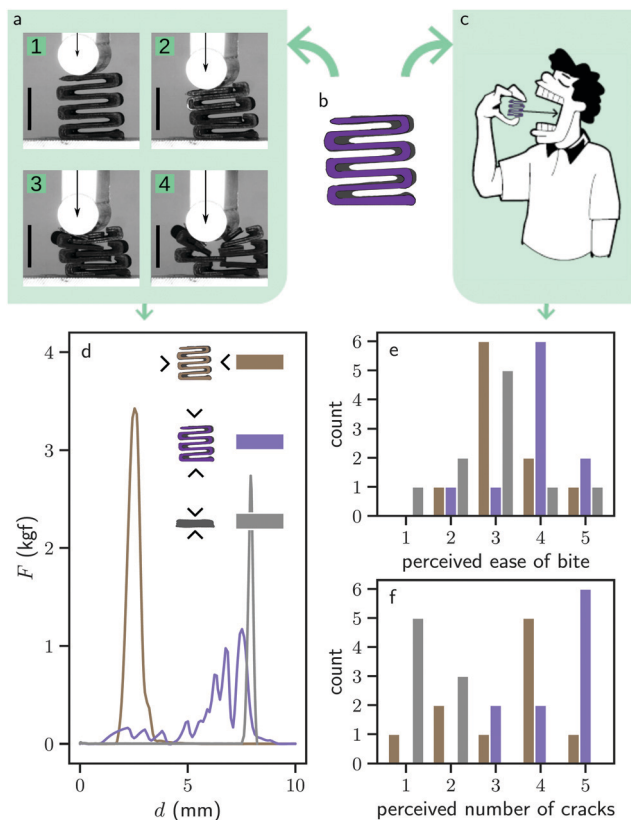


Fig. 1 Anisotropic edible mechanical metamaterials. In panel a, several frames show the step-by-step compression of the S-structure shown in b, at a compressive displacement of 0 mm (1), 3 mm (2), 5 mm (3) and 7 mm (4). The scale bar is 10 mm. These frames were recorded during a uniaxial compression test, whose results are shown in panel d. These tests were followed up by sensory experiments, as indicated in panel c. Panels e and f show histograms comparing the perceived mechanical properties (ease of bite for panel e and perceived number of cracks for panel f) of the chocolate S-structure when bit in two different directions, relative to the reference shape. A Fisher test on the data of panel e (resp. f) reveals that there is a $p = 3\%$ (resp. $p = 9\%$) probability that the ease of bite (resp. the number of cracks) of the sample in the horizontal direction is greater than 3 (resp. 4), while the ease of bite (resp. the number of cracks) of the sample in the vertical direction is smaller than or equal to 3 (resp. 4).

that of the reference geometry. It is also brittle, as the force-displacement curve exhibits a single peak. In contrast, when the structure is compressed along its vertical direction, the mechanical metamaterial is much softer, as its stiffness (strength) is 40 (25) times lower than in the horizontal direction (see Table II of the Methods). In addition, it is also less brittle, as the force-displacement curve exhibits a finite force for larger range of compressive displacements and multiple peaks. Thus, the mechanical metamaterials exhibits a strong anisotropic fracture response, which is difficult to realize in typical food microstructures.²⁰

To investigate whether this stark contrast in mechanical properties between the two orientations leads to a noticeable difference in perceived mouthfeel experience, we perform a sensory assessment on a batch of 10 persons—see Methods for details about the sensory assessment protocol. The results suggest that a noticeable difference in ease of bite is perceived between the two orientations of the mechanical metamaterial

(Fig. 1e). A Fisher test for statistical relevance reveals that the mechanical metamaterial in the horizontal direction is systematically perceived as having an ease of bite lower than 3 whereas the mechanical metamaterial in the vertical direction is systematically perceived as having an ease of bite greater than or equal to 3—we find a significance level $p = 3\%$. In contrast, a similar Fisher test reveals that both mechanical metamaterials have a comparable perceived number of cracks (Fig. 1f, we find a significance level of $p = 9\%$, which exceeds the commonly used $p = 5\%$ threshold needed to claim statistical relevance²¹). To conclude, we observe a statistically significant correlation between the anisotropic strength of the mechanical metamaterials and the anisotropy in the ease of bite. An additional interesting feature is that the strong direction of the mechanical metamaterials has larger strength and comparable ease of bite than that of the reference, even though the volume density of the mechanical metamaterials is 64% (see Table II of the Methods), which is significantly lower than the 100% volume density of the reference structure.

Design of crack number

Which additional mouthfeel experiences can we tune with mechanical metamaterials? Inspired by the multiple local maxima of the mechanical metamaterial in the vertical orientation and the slightly larger perceived number of cracks in Fig. 1f, we design an additional set of mechanical metamaterials in which the number of fracture and self-contact events can be tuned by geometry. We design a spiral-shaped mechanical metamaterial in which the number of windings of the spiral n can be tuned from 1 to 3 (see Fig. 2a–c). Upon compression, the force-displacement curve exhibits drastic changes. First, the strength of the mechanical metamaterial increases from 8.3×10^{-2} kgf to 4.8×10^{-1} kgf, which is consistent with the fact that the volume fraction increases with the winding number n (see Table II of the Methods).

In addition, the force-displacement curves exhibit subsequent local maxima and local minima. Such maxima correspond to local fracture events whereas the local minima correspond to reconfigurations of the mechanical metamaterial ensued by the creation of self-contacts. The number of local fractures increases with the winding number n . In addition to quantifying the number of fracture events, we also recorded sound during the experiments and detected fracture events using the sound waveform. Such sound is also expected to be an integral part of the sensory experience during biting.²² We find that the number of fracture events detected with sound exhibits a positive correlation with that of the force-displacement curve (Fig. 2g). In addition to the sound recording, we also performed a sensory assessment with these mechanical metamaterials (see Methods for details on the protocol). We observe that both the overall sensory rating (Fig. 2h) as well as the perceived number of cracks (Fig. 2i) exhibit a positive correlation with the number of cracks measured from the force-displacement curve. This positive correlation is partially confirmed by Fisher statistical relevance tests, which confirm the S-shaped mechanical metamaterials with $n = 2$ and $n = 3$ have a larger perceived number of cracks than the one with $n = 1$. This is surprising given the large differences in boundary conditions



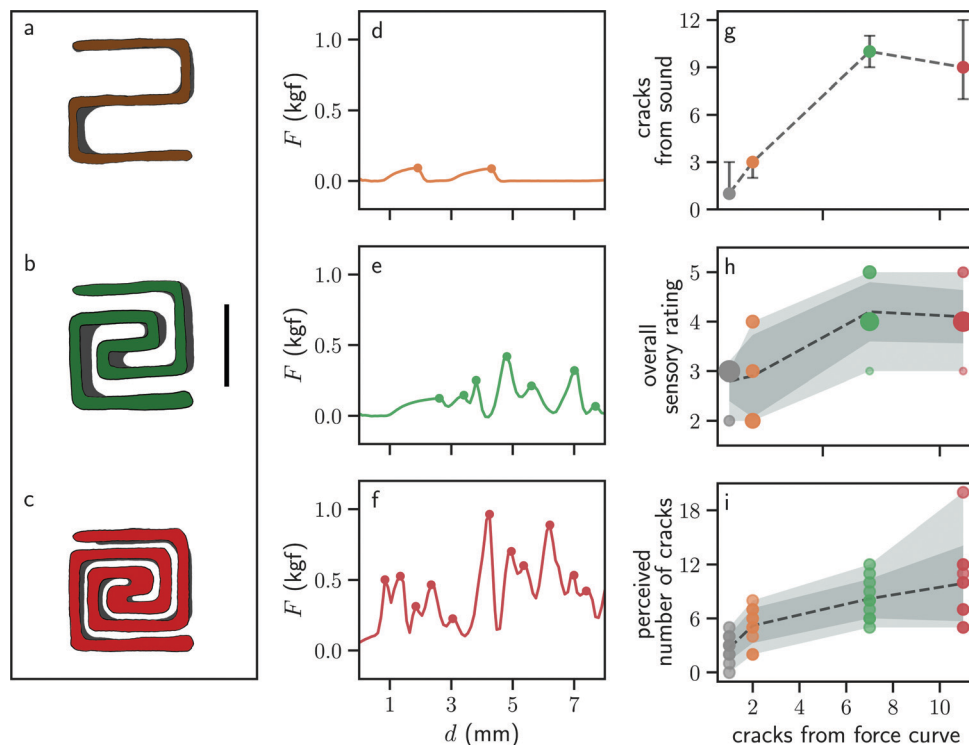


Fig. 2 Edible mechanical metamaterials with tunable numbers of cracks. Panels a–c show the spiral-shaped mechanical metamaterials with a winding number $n = 1$ (a), $n = 2$ (b) and $n = 3$ (c). The scale bar is 10 mm. Panels d–f show the corresponding force-curves obtained from the uniaxial compression experiments for $n = 1$ (d), $n = 2$ (e) and $n = 3$ (f). Colored dots indicate drops in the applied force, interpreted as the formation of individual cracks. Panels g–i show correlations between the number of cracks extracted from the force-curves and several factors: in g, we plot them against the number of peaks extracted from the audio recordings; in h and i, this data is correlated with the overall rating and the perceived number of cracks, respectively, as assessed by our sensory study. The dashed black line connects the average points and the darker shaded region represents the standard deviation around this average. In panel h, the size of the dot is proportional to the number of occurrences. Fisher tests on the data of panel i reveal that the probabilities that the mechanical metamaterials with $n = 1$ have a perceived number of cracks that is greater than 3 while the perceived number of cracks mechanical metamaterials with $n = 2$ and $n = 3$ is less than or equal to 3 are both $p = 0\%$. The probability that the mechanical metamaterials with $n = 2$ have a perceived number of cracks that is greater than 4 while the perceived number of cracks mechanical metamaterials with $n = 3$ is less than or equal to 4 is $p = 8\%$.

between the mechanical test—realized with ideal boundary conditions—and the sensory assessment, where there is inevitable variability in the loading conditions while biting.

Topology optimization of anisotropic fracture resistance

Now that we have shown that mechanical metamaterials with different fracture properties can lead to different mouthfeel experiences and even improve the overall tasting experience, we push their rational design one step further by using topology optimization to create maximally anisotropic structures. We devise an optimization problem that minimizes a quantity J_1 when compressing the mechanical metamaterial in the vertical y direction and simultaneously maximizes another quantity J_2 when compressing it in the horizontal x direction. J_1 and J_2 aggregate the energy release rates of every potential crack along the structural boundary. These are then combined into a single objective function $J = \omega J_1 - (1 - \omega) J_2$, in which $0 \leq \omega \leq 1$ is a weight parameter. The multiobjective optimization problem has therefore been cast as a single objective problem using a simple weighted sum—see Methods for details about the computational approach.

We run our topology optimization algorithm for multiple values of ω with a fixed volume fraction of 50%. As this volume

constraint could become inactive when ω approaches zero, setting a bound on the volume may not be enough to guarantee a design with the target 50% volume fraction. Instead, we use two bounds and constrain the volume fraction to lie between 49.9% and 50.1%. For a value $\omega = 0$, only the second term in J is non-zero, resulting in an optimized topology that is very brittle when compressed along x . Conversely, for $\omega = 1$ only the first term in J is non-zero, with an optimized topology that makes the mechanical metamaterial very tough along y . Although the algorithm optimizes for fracture resistance, since chocolate is brittle, we expect the enhanced fracture anisotropy to also manifest itself *via* an enhanced strength anisotropy.²³ Five optimized designs were 3D-printed in chocolate (Fig. 3a) and their mechanical properties were tested (Fig. 3b–f)—See Methods for printing and test protocols. The mechanical tests reveal that all structures have a similar force-displacement curve. Initial stiffness and maximum strength values are reported in Table II of the Methods; the maximum strength was obtained at compressive displacements between 1 and 2 mm. As expected, we find that the mechanical metamaterial displays a maximally anisotropic strength for $\omega = 0.5$ (Fig. 3). This result can be interpreted from the geometry of the mechanical metamaterial, which has thin necks in the x direction and



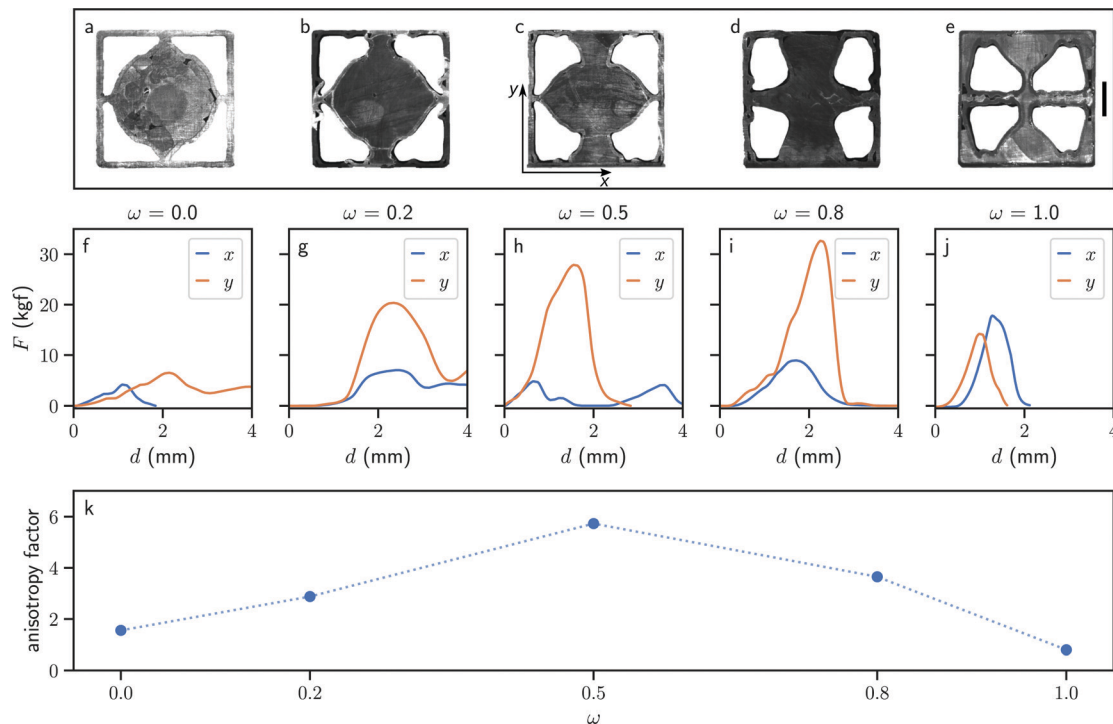


Fig. 3 Design of different anisotropic edible mechanical metamaterials with topology optimization. Panels (a–e) display the mechanical metamaterials generated by topology optimization and 3D printed with chocolate. The scale bar is 10 mm. Panel (a–e) correspond to the weights $\omega = 0, 0.2, 0.5, 0.8$ and 1 , respectively. We plot in panels (f–j) the corresponding force-displacement curves extracted from the uniaxial compression tests in the x (blue) and y (orange) directions. Panel (f–j) correspond to the weights $\omega = 0, 0.2, 0.5, 0.8$ and 1 , respectively. Finally, panel (k) plots the anisotropy factor as a function of the tuning parameter ω . This anisotropy factor is defined as the quotient between the peak forces measured for each direction.

thick walls in the y direction. Such strong anisotropy is twice as large as that of the structure in Fig. 1, therefore we expect it to have to a strong ease of bite anisotropy.

Conclusions

To conclude, by designing, performing mechanical tests and carrying out sensory assessments of a range of edible mechanical metamaterials, we have shown that it is possible to control some features of the mouthfeel sensory experience, such as the perceived ease of bite and perceived number of cracks upon biting. We have further established that topology optimization is a powerful route to obtain metamaterials with on-demand anisotropy. Our work opens the door to new approaches for rational design of human-matter interactions and of fracture properties by using optimization methods for fracture, for edible products, but also engineering structures and beyond.

Methods

Design approach

Due to the limitations imposed by the printing process—see 3D printing for a description of these—we decided to focus on geometries in which each layer could be printed in one continuous strand. These factors constrained us to the shapes shown on Fig. 1b and 2a–c. The various spirals were drawn in FreeCAD,

an open-source and freely available CAD software package, whereas the S-structure is simply one of the predefined patterns available in Visual Machines, the control software for Envision-TEC's 3D-Bioplotter. Whereas the latter contains several parallel beams, giving rise to its anisotropic properties, the spirals' interesting mouthfeel is less dependent on the biting direction. Overall, both designs rely on the same principle: the addition of breakable elements such as beams perpendicular to the direction of compression should result in a richer feeling in the mouth.

Not only do the spirals possess a large number of breakable elements, the variable winding number (n) provides an obvious tuning parameter to find the sweet spot in terms of sensory perception. Initially, we tested winding numbers up to $n = 7$ for larger pieces but when printing bite-sized samples for the sensory study, we realized that $n > 3$ wasn't printable given the limited resolution—see 3D printing for an explanation. In the end, we arrived at $15 \times 15 \times 10 \text{ mm}^3$ for the dimensions of the spirals and the S-structure. The reference shape is $15 \times 15 \times 4 \text{ mm}^3$, making it thinner than the other shapes. This was done in an attempt to match the overall amount of chocolate deposited between different geometries.

3D printing

3D printing chocolate proved to be a challenging endeavor, due to the material's polymorphism.²⁴ There are 6 different crystal forms of chocolate, each with their own mechanical properties and melting points. Typical chocolate products favor form V



crystals, which tend to be shiny and smooth, producing audible snaps when bitten into.²⁵ This particular crystal form melts at 34 °C²⁶ so the working temperature of the chocolate must be kept under this value. We used Cacao Barry's Venezuela 72% dark chocolate, due to its advertised fluidity and high concentration of cacao—lower purity levels would further complicate the tempering and printing processes.

Tempering was achieved using the seeding method, which consists of the following steps:

- Bring the chocolate temperature above the highest melting point of its different crystal forms (36 °C for form VI crystals). To ensure fully melted chocolate, we heated the material up to 45 °C.
- When the desired temperature is reached, turn the heating device off.
- Proceed to gradually add solid pellets of pre-tempered chocolate, stirring carefully, while monitoring the temperature of the liquid.

Table 1 Parameters used in the 3D printing process. Due to fluctuations in chocolate fluidity, the nozzle speed and extrusion pressure required frequent recalibration and adjustment

Syringe temperature (°C)	32
Platform temperature (°C)	12
Nozzle diameter (mm)	1.2
Nozzle speed (mm s ⁻¹)	15–40
Extrusion pressure (bar)	0.1–2

Table 2 Summary of some mechanical properties of the different designs

Sample	Strength (kgf)	Stiffness (kgf mm ⁻¹)	Volume fraction
S-Structure (x)	3.41	4.11	0.64
S-Structure (y)	0.148	0.112	0.64
Reference	2.66	6.19	1.0
Spiral (n = 1)	0.0832	0.0761	0.32
Spiral (n = 2)	0.108	0.0613	0.48
Spiral (n = 3)	0.484	0.364	0.64
TO, ω = 0.0 (x)	4.23	3.99	0.50
TO, ω = 0.0 (y)	6.47	3.04	0.50
TO, ω = 0.2 (x)	7.00	3.89	0.50
TO, ω = 0.2 (y)	20.3	11.6	0.50
TO, ω = 0.5 (x)	4.76	7.41	0.50
TO, ω = 0.5 (y)	27.7	17.6	0.50
TO, ω = 0.8 (x)	8.84	6.08	0.50
TO, ω = 0.8 (y)	32.6	16.3	0.50
TO, ω = 1.0 (x)	17.7	21.4	0.50
TO, ω = 1.0 (y)	14.2	15.4	0.50

Table 3 Results obtained from the sensory study, summarizing how the different shapes were perceived, across different categories: crunchiness, ease of bite and overall rating, on a scale of 1–5, and the absolute estimated number of cracks. The estimated number of cracks was then normalized according to eq:norm. We present the averaged values across all participants in the “Av.” subcolumns and the standard deviations in the “Dev.” subcolumns

Sample	Reference		Sp. (n = 1)		Sp. (n = 2)		Sp. (n = 3)		S-str. (x)		S-str. (y)		S-str. (z)	
	Av.	Dev.	Av.	Dev.	Av.	Dev.	Av.	Dev.	Av.	Dev.	Av.	Dev.	Av.	Dev.
Crunchiness	2.3	0.6	3.1	1.2	4.0	0.9	4.2	0.9	3.7	0.9	4.0	1.0	3.3	1.0
Ease of bite	2.9	1.0	4.3	0.9	4.1	0.5	3.5	0.8	3.3	0.8	3.9	0.8	3.1	1.1
Normalized cracks	1.1	0.6	2.2	0.6	3.6	0.8	4.1	0.9	3.2	1.1	4.3	1.0	2.4	0.9
Overall rating	2.8	0.4	2.9	0.8	4.2	0.6	4.1	0.5	3.5	0.5	4.0	0.4	3.0	1.0

- When the temperature drops below the aforementioned melting point for form V crystals (34 °C), the chocolate is now ready to be printed.

The seeding process ensures that the right crystals are dispersed into the mix, acting as nucleation sites for further growth of the desired crystal form.

After tempering, the chocolate is loaded onto a syringe which is then inserted in the 3D-Bioplotter's heated cartridges, which are kept at 32 °C. To make sure that, after deposition, solidification happens as quickly as possible, the printing base is kept at 12 °C and a simple fan is used to create air flow.

In extrusion-based 3D printing, smaller nozzles are preferred due to the higher resolution they allow for, but we quickly realized that if the nozzle was too small, it would easily get blocked by the growing nucleation sites dispersed in the chocolate. So, we had a relatively large (1.2 mm) nozzle custom made, which worked effectively most of the time—we circumvented the limited resolution by working with single walled designs.

The 3D-Bioplotter uses air pressure to extrude the printing material. This means that a balance between air pressure and nozzle speed must be struck. We found that there was no consistent way to strike this balance, as the fluidity of chocolate seems to fluctuate when it is left unstirred inside the syringe. A printing session would often start with relatively low pressures (0.1 bar) and high speeds (40 mm s⁻¹) but, as the chocolate thickened, we were forced to increase the pressure and to reduce the speed. Needless to say, the printing process requires frequent calibration to ensure that the printed lines have approximately constant thickness—matching the diameter of the nozzle.

Another common issue, related to the inconsistent fluidity of chocolate described here, was the over- or under-deposition of material at the beginning and end of each printed line. This too was calibrated and accounted for as much as possible, but unpredictable factors, such as the size of the droplet left on the nozzle after printing, made it challenging to fully eliminate this factor. Hence, we decided to focus on continuous strand designs, such that each layer could be printed in one go, leaving only two possible sites for the formation of irregularities (the beginning and the end of each line) (Tables 1–3).

Mechanical testing

Testing was done using an Instron 5943 uniaxial compression device. The samples were placed on a flat bed and crushed by a cylindrical rod attached to the movable arm of the machine; a



constant compression speed of 5 mm s^{-1} was set. A 500 N load cell was used to register the force applied by the aforementioned cylindrical rod.

During the compression, a Basler acA2040-90 μm camera was used to record pictures of the process, while a MiniDSP UMIK-1 microphone was used to capture audio.

The different samples were kept refrigerated right until the moment of testing, to ensure temperature uniformity across all tests.

Sensory assessment

The sensory study was performed by a panel of 10 untrained volunteers, recruited *via* email. The group was composed of students, researchers and technical staff, all unaware of the purpose of the study. Upon arrival in the testing room, they were provided with a printed questionnaire, containing instructions on how to handle and bite the pieces using their molars. The participants were also instructed to close their jaws at a deliberately slow pace, in an effort to match the conditions of the sensory study to those of the mechanical tests. Furthermore, the different samples were kept refrigerated until the moment of testing, spending only a few seconds exposed to the room temperature before being ingested. The order in which the samples were presented was randomized and each was assigned a codename, so as not to introduce any biases in its perceived properties. Between trials, the participants were allowed to take breaks to cleanse their palates with tap water. The participants were allowed to try each piece more than once, if necessary, to get a better sense of its characteristics. The participants were asked to focus specifically on the first bite, filling in their answers for each question based on their impressions of this experience.^{12,27} They were asked to rate each sample with a number between 1 and 5 for each of the following questions:

- How crunchy was it?
- How easy was it to bite?
- How would you rate the overall experience?

Finally, the participants were asked to estimate the absolute number of cracks felt. The results for this particular question were then normalized as follows:

$$\bar{a}_i = 5 \times \frac{a_i}{\max(a_1, a_2, \dots)} \quad (1)$$

Here, \bar{a}_i and a_i are, respectively, the normalized and absolute values of the estimated number of cracks for a given sample i . This normalization was chosen to take into account different individual criteria for what counts as a crack. Note that the perceived ease of bite is related to the perceived thickness in the case of liquid products,¹² which is the force needed to make the sample flow or deform in the mouth.

Topology optimization

Topology optimization (TO)^{28,29} is a technique widely used in structural optimization that combines finite element analysis (FEA) with a gradient-based optimizer. Starting with a computational domain, the procedure seeks the most appropriate

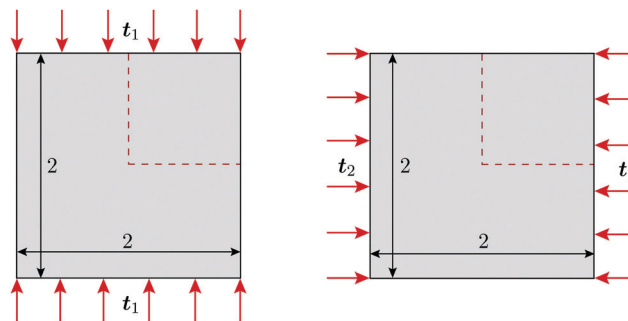


Fig. 4 A domain with dimension 2×2 under compression, where \mathbf{t}_1 and \mathbf{t}_2 are prescribed on the vertical and horizontal directions, respectively. Under the finite element analysis, a quarter of domain (marked with red dashed segments) is considered.

material layout to minimize a given objective function subject to given constraints. In this work we use TO to tailor fracture resistance³⁰ and thus introduce anisotropy into the mechanical metamaterial structure to that end, we use two loading cases as shown in Fig. 4. Due to symmetry, we consider only a quarter of the domain during the optimization. Our objective function thus minimizes some measure of the energy release rate J_1 when compressing the mechanical metamaterial in the vertical direction, while maximizes another value J_2 when compressing along the horizontal direction. The optimization, which is also subject to a volume constraint of chocolate, is mathematically defined as

$$\begin{aligned} &\text{minimize} && J = \omega J_1 - (1 - \omega) J_2 \\ &\text{such that} && \mathbf{K}_1 \mathbf{U}_1 = \mathbf{F}_1, \\ &&& \mathbf{K}_2 \mathbf{U}_2 = \mathbf{F}_2, \\ &&& V_{c1} \leq V_{\text{solid}}, \\ &&& V_{\text{solid}} \leq V_{c2}, \end{aligned} \quad (2)$$

where J_i is computed after solving its associated discrete finite element equilibrium equation $\mathbf{K}_i \mathbf{U}_i = \mathbf{F}_i, i = 1, 2$, and $0 \leq \omega \leq 1$ is a weight factor that essentially transforms a two-objective optimization problem into a single one. V_{solid} is the volume fraction of solid material, and V_{c1} and V_{c2} are the corresponding lower and upper bounds, which are set to 49.9% and 50.1%, respectively. After solving the i th discrete problem, J_i is computed as

$$J_i = \frac{1}{N} \sum_{j=1}^N G_j, \quad (3)$$

where N is the number of nodes along chocolate-void interfaces, and G_j is the energy release rates of the j th node, which is approximated using topological derivatives³¹ as

$$G_j = \frac{\pi \eta}{E} \boldsymbol{\sigma}_j^T \mathbf{Q}(\gamma, \beta) \boldsymbol{\sigma}_j. \quad (4)$$

In this equation, $\boldsymbol{\sigma}_j$ is Cauchy's stress evaluated at a node, and $\bar{E} = E/(1 - \nu^2)$ for plane strain conditions, in which E is Young's



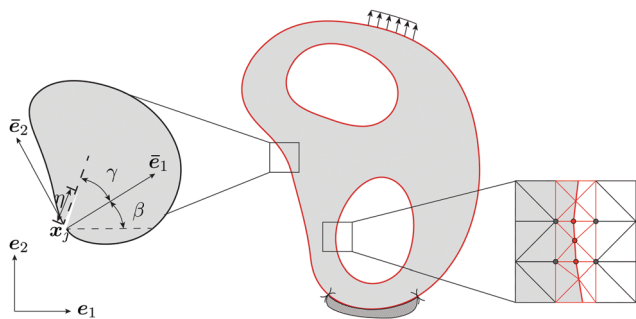


Fig. 5 The illustration of a crack with length η nucleating at node j , where γ is the angle between this crack and the internal normal of structural boundary, and β is the angle between the global coordinate system and local coordinate system located at node j . Enriched nodes (marked with red circles) are detected at intersections with between structural boundaries and the edge of elements, and integration elements are created near the boundary.

modulus and ν is Poisson's ratio. As shown in Fig. 5, a crack nucleating at a chocolate–void interface has length η and angle γ , the latter measured from the normal vector to the interface; β is the angle between the global coordinate system (marked in red) and the local coordinate system positioned at node x_j . Finally, Q is a matrix that is function of angles γ and β , whose details are given in the appendix. According to eqn (4), the evaluation of energy release rates uses the stress field; locations along the structural boundary with high (tensile) stress exhibit high values of energy release rate and

could therefore lead to crack nucleation. The connection between high stresses and crack nucleation has been used elsewhere to predefine cracks at the beginning of topology optimization.^{32,33}

Our approach to topology optimization^{30,34} uses a level set function φ , whose zeroth value represents the interface between chocolate and void, an enriched finite element formulation to accurately determine the structural response, and the method of moving asymptotes (MMA) as the optimizer to update design variables. Noteworthy, energy release rates are computed at the locations of enriched nodes that are added to the finite element formulation to properly describe the discontinuous kinematics at void–solid interfaces. In comparison with standard density-based TO methods, our approach can provide smooth and crisp designs without the need for post-processing.^{30,34}

Fig. 6 shows the initial design containing four circular holes within the entire mechanical metamaterial cell (only one hole in our quarter optimization domain), where the ratio $J_2/J_1 = 1$. Starting from this initial design, the final optimized designs for different values of ω are shown in the same figure. As ω increases, more emphasis is placed on minimizing J_1 , which leads to more solid material being placed along the vertical direction. Conversely, as ω decreases, the designs that minimize $-J_2$ (or maximize J_2) have weak bars in the horizontal direction—thus maximizing energy release rates. Maximum anisotropy is attained for $\omega = 0.5$, *i.e.*, $J_2/J_1 = 14.85$. Fig. 7 shows the convergence of J_1 , J_2 , and V_{solid} , where it can be seen that J_1 increases and J_2 decreases throughout the

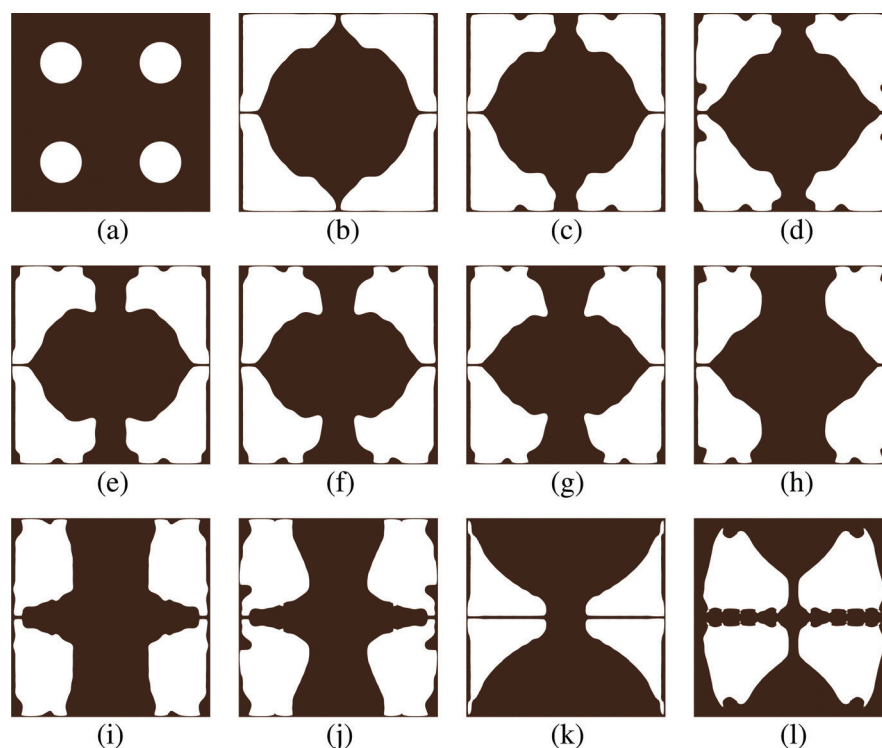


Fig. 6 (a) Initial design with four holes in the whole design domain; (b)–(l) Final designs with different weights $\omega = 0, 0.1, \dots, 1$.



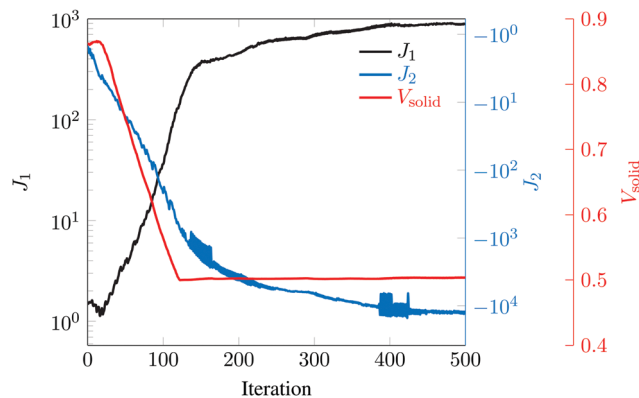


Fig. 7 Convergence of J_1 , J_2 , and V_{solid} for $\omega = 0.5$.

optimization process, and that the material volume fraction V_{solid} converges to 50%. Since the magnitude of J_2 is larger than that of J_1 , the optimizer gives priority to the former. Since optimized designs depend on the initial topology—because we use gradient information starting from the initial

$$\begin{aligned}
 H_{11}(\gamma) &= \sum_{i=1}^6 \left\{ [1 - \tan(\gamma)^2] \cdot c_i^{(I,1)} \cos[(i-1)\gamma] - \frac{\sin(\gamma)}{\cos(\gamma)^3} \cdot c_i^{(I,2)} \sin(i\gamma) \right\} \\
 H_{12}(\gamma) &= \sum_{i=1}^6 \left\{ 2 \tan(\gamma) \cdot c_i^{(I,1)} \cos[(i-1)\gamma] + \frac{1}{\cos(\gamma)^2} \cdot c_i^{(I,2)} \sin(i\gamma) \right\} \\
 H_{21}(\gamma) &= \sum_{i=1}^6 \left\{ [1 - \tan(\gamma)^2] \cdot c_i^{(II,1)} \sin(i\gamma) - \frac{\tan(\gamma)}{\cos(\gamma)^2} \cdot c_i^{(II,2)} \cos[(i-1)\gamma] \right\} \\
 H_{22}(\gamma) &= \sum_{i=1}^6 \left\{ 2 \tan(\gamma) \cdot c_i^{(II,1)} \sin(i\gamma) + \frac{1}{\cos(\gamma)^2} \cdot c_i^{(II,2)} \cos[(i-1)\gamma] \right\},
 \end{aligned} \tag{8}$$

design—to study the variability in final designs we also looked at other initial layouts for $\omega = 0.5$. The results of this study are given in Fig. 8, where we see that optimized structures are different than that shown in Fig. 6(f)—although the main features are retained. It should also be mentioned that optimized designs are also sensitive to the move limit used in MMA.

Formulation of the topology optimization

Following the work of Silva *et al.*³¹ on topological derivatives, the matrix \mathbf{Q} in eqn (4) is given by

$$\mathbf{Q}(\gamma, \beta) = \mathbf{O}(\beta)^T \mathbf{P}(\gamma)^T \mathbf{H}^T(\gamma) \mathbf{H}(\gamma) \mathbf{P}(\gamma) \mathbf{O}(\beta). \tag{5}$$

In this equation, $\mathbf{O}(\beta)$ is a transformation matrix for translating global to local stresses along the boundary, defined as

$$\mathbf{O}(\beta) = \begin{bmatrix} c^2 & sc & sc & s^2 \\ -sc & c^2 & -s^2 & sc \\ -sc & -s^2 & c^2 & sc \\ s^2 & -sc & -sc & c^2 \end{bmatrix}, \tag{6}$$

where $c = \cos \beta$ and $s = \sin \beta$. $\mathbf{P}(\gamma)$ is used to obtain stresses in polar coordinates, and it is given by

$$\mathbf{P}(\gamma) = \begin{bmatrix} s^2\gamma & \frac{\sin 2}{2} & \frac{\sin 2\gamma}{2} & c^2 \\ -sc & \frac{c^2 - s^2}{2} & \frac{c^2 - s^2}{2} & sc \end{bmatrix}, \tag{7}$$

where this time $c = \cos \gamma$ and $s = \sin \gamma$. As stated in the work of Beghini *et al.*,³⁵ $\mathbf{H}(\gamma)$ is a 2×2 matrix associated with angle γ , with components

where $c_i^{(I,1)}$, $c_i^{(II,1)}$, $c_i^{(I,2)}$, and $c_i^{(II,2)}$ are given in Table 4.

Sensitivity

The sensitivity of the objective function J with respect to a design variable σ is derived by using the adjoint variable method. The Lagrangian function of the objective constructed

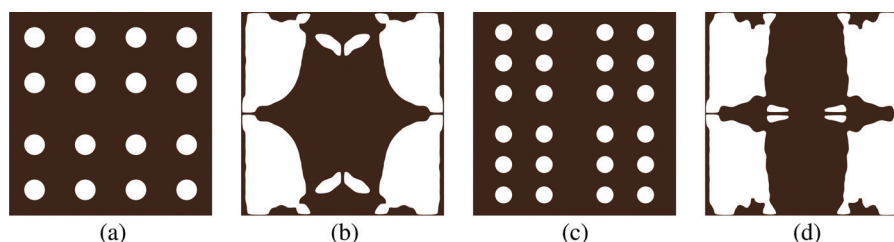


Fig. 8 (a and c) Initial designs with 16 holes and 24 holes, and (b and d) the corresponding final results obtained with $\omega = 0.5$.



Table 4 Data of parameters $c_i^{(l,1)}$, $c_i^{(ll,1)}$, $c_i^{(l,2)}$, and $c_i^{(ll,2)}$ in matrix $\mathbf{H}(\gamma)$

i	$c_i^{(l,1)}$	$c_i^{(ll,1)}$	$c_i^{(l,2)}$	$c_i^{(ll,2)}$
1	-0.174856	-0.198196	-0.419098	0.478653
2	1.393783	0.681479	-0.197271	-0.130868
3	-0.278259	-0.282608	-0.445897	0.663435
4	0.240695	0.136522	-0.050066	-0.066599
5	-0.071883	-0.041562	-0.022856	0.183693
6	0.011246	0.006177	0.003281	-0.006140

by using the adjoint vectors λ_1 and λ_2 is expressed as

$$L = J + \lambda_1^T (\mathbf{K}_1 \mathbf{U}_1 - \mathbf{F}_1) + \lambda_2^T (\mathbf{K}_2 \mathbf{U}_2 - \mathbf{F}_2). \quad (9)$$

Then the derivative of L with respect to the j th design variable s_j is given by

$$\begin{aligned} \frac{dL}{ds_j} = & \omega \frac{\partial J_1}{\partial s_j} - (1 - \omega) \frac{\partial J_2}{\partial s_j} \\ & + \lambda_1^T \frac{\partial \mathbf{K}_1}{\partial s_j} \mathbf{U}_1 - \lambda_1^T \frac{\partial \mathbf{F}_1}{\partial s_j} \\ & + \lambda_2^T \frac{\partial \mathbf{K}_2}{\partial s_j} \mathbf{U}_2 - \lambda_2^T \frac{\partial \mathbf{F}_2}{\partial s_j} \\ & + \left(\omega \frac{\partial J_1}{\partial \mathbf{U}_1} + \lambda_1^T \mathbf{K}_1 \right) \frac{\partial \mathbf{U}_1}{\partial s_j} \\ & + \left(-(1 - \omega) \frac{\partial J_2}{\partial \mathbf{U}_2} + \lambda_2^T \mathbf{K}_2 \right) \frac{\partial \mathbf{U}_2}{\partial s_j}. \end{aligned} \quad (10)$$

After obtaining the adjoint vectors λ_1 and λ_2 by solving the following adjoint equations

$$\omega \frac{\partial J_1}{\partial \mathbf{U}_1} + \lambda_1^T \mathbf{K}_1 = 0, \quad (11)$$

and

$$-(1 - \omega) \frac{\partial J_2}{\partial \mathbf{U}_2} + \lambda_2^T \mathbf{K}_2 = 0, \quad (12)$$

the above sensitivity formulation is simplified as

$$\begin{aligned} \frac{dL}{ds_j} = & \omega \frac{\partial J_1}{\partial s_j} - (1 - \omega) \frac{\partial J_2}{\partial s_j} \\ & + \lambda_1^T \frac{\partial \mathbf{K}_1}{\partial s_j} \mathbf{U}_1 - \lambda_1^T \frac{\partial \mathbf{F}_1}{\partial s_j} \\ & + \lambda_2^T \frac{\partial \mathbf{K}_2}{\partial s_j} \mathbf{U}_2 - \lambda_2^T \frac{\partial \mathbf{F}_2}{\partial s_j}. \end{aligned} \quad (13)$$

According to eqn (3) and (4), the derivative $\partial J_i / \partial \mathbf{U}_i$, $i = 1, 2$ can be expressed as

$$\frac{\partial J_i}{\partial \mathbf{U}_i} = \frac{1}{N} \sum_{j=1}^N \frac{\partial G_j}{\partial \mathbf{U}_i}, \quad (14)$$

where

$$\begin{aligned} \frac{\partial G_j}{\partial \mathbf{U}_i} = & \frac{\pi \varepsilon}{E} \frac{\partial \left(\boldsymbol{\sigma}_j^T \mathbf{Q}(\gamma, \beta) \boldsymbol{\sigma}_j \right)}{\partial \mathbf{U}_i} \\ = & \frac{\pi \varepsilon}{E} \left(\frac{\partial \boldsymbol{\sigma}_j^T}{\partial \mathbf{U}_i} \mathbf{Q}(\gamma, \beta) \boldsymbol{\sigma}_j + \boldsymbol{\sigma}_j^T \mathbf{Q}(\gamma, \beta) \frac{\partial \boldsymbol{\sigma}_j}{\partial \mathbf{U}_i} \right). \end{aligned} \quad (15)$$

The stress of j th node, $\boldsymbol{\sigma}_j$, is defined as

$$\boldsymbol{\sigma}_j = \frac{\sum_{e=1}^{N_e} \mathbf{D} \mathbf{B}_e \mathbf{U}_i}{N_e}, \quad (16)$$

where N_e is the number of elements sharing the j th node, \mathbf{D} is the constitutive tensor, and \mathbf{B}_e is the strain-displacement matrix. Then, its derivative with respect to the displacement field \mathbf{U}_i is given by $\boldsymbol{\sigma}_j$

$$\frac{\partial \boldsymbol{\sigma}_j}{\partial \mathbf{U}_i} = \frac{\sum_{e=1}^{N_e} \mathbf{D} \mathbf{B}_e}{N_e}. \quad (17)$$

Conflicts of interest

There are no conflicts to declare.

Acknowledgements

We thank A. Deblais for insightful discussions and suggestions, S. Koot and D. Giesen for technical assistance. We acknowledge funding from an IXA Physics2market grant. C. C. acknowledges funding from the European Research Council *via* the Grant ERC-StG-Coulais-852587-Extr3Me. All the codes and data supporting this study are available on the public repository <https://doi.org/10.5281/zenodo.4632399>.

References

- 1 M. Kadic, T. Bückmann, R. Schittny and M. Wegener, Metamaterials beyond electromagnetism, *Rep. Prog. Phys.*, 2013, **76**(12), 126501.
- 2 K. Bertoldi, V. Vitelli, J. Christensen and M. van Hecke, Flexible mechanical metamaterials, *Nat. Rev. Materials*, 2017, **2**(11), 17066.
- 3 D. M. Kochmann and K. Bertoldi, Exploiting Microstructural Instabilities in Solids and Structures: From Metamaterials to Structural Transitions, *Appl. Mech. Rev.*, 2017, **69**(5), 050801.
- 4 X. Zheng, W. Smith, J. Jackson, B. Moran, H. Cui and D. Chen, *et al.*, Multiscale metallic metamaterials, *Nat. Mater.*, 2016, **15**(10), 1100–1106.
- 5 S. Shan, S. H. Kang, J. R. Raney, P. Wang, L. Fang and F. Candido, *et al.*, Multistable Architected Materials for Trapping Elastic Strain Energy, *Adv. Mater.*, 2015, **27**(29), 4296–4301.



- 6 T. Chen, M. Pauly and P. M. Reis, A reprogrammable mechanical metamaterial with stable memory, *Nature*, 2021, **589**(7842), 386–390.
- 7 C. Coulais, E. Teomy, K. de Reus, Y. Shokef and M. van Hecke, Combinatorial design of textured mechanical metamaterials, *Nature*, 2016, **535**(7613), 529–532.
- 8 M. M. Driscoll, B. G. Chen, T. H. Beuman, S. Ulrich, S. R. Nagel and V. Vitelli, The role of rigidity in controlling material failure, *Proc. Natl. Acad. Sci. U. S. A.*, 2016, **113**(39), 10813–10817.
- 9 N. P. Mitchell, V. Koning, V. Vitelli and W. T. Irvine, Fracture in sheets draped on curved surfaces, *Nat. Mater.*, 2017, **16**(1), 89–93.
- 10 C. Bonatti and D. Mohr, Mechanical performance of additively-manufactured anisotropic and isotropic smooth shell-lattice materials: simulations & experiments, *J. Mech. Phys. Solids*, 2019, **122**, 1–26.
- 11 M. H. Tunick, C. I. Onwulata, A. E. Thomas, J. G. Phillips, S. Mukhopadhyay and S. Sheen, *et al.*, Critical Evaluation of Crispy and Crunchy Textures: A Review, *Int. J. Food Properties*, 2013, **16**(5), 949–963.
- 12 A. Deblais, E. D. Hollander, C. Boucon, A. E. Blok, B. Veltkamp and P. Voudouris, *et al.*, Predicting thickness perception of liquid food products from their non-Newtonian rheology, *Nat. Commun.*, 2021, **12**(1), 6328.
- 13 M. Aguayo-Mendoza, M. Santagiuliana, X. Ong, B. Piqueras-Fiszman, E. Scholten and M. Stieger, How addition of peach gel particles to yogurt affects oral behavior, sensory perception and liking of consumers differing in age, *Food Res. Int.*, 2020, **134**, 109213.
- 14 A. van Eck, A. van Stratum, D. Achlada, B. Goldschmidt, E. Scholten and V. Fogliano, *et al.*, Cracker shape modifies ad libitum snack intake of crackers with cheese dip, *Br. J. Nutr.*, 2020, **124**(9), 988–997.
- 15 A. Piovesan, V. Vancauwenberghe, W. Aregawi, M. A. Delele, E. Bongaers and M. de Schipper, *et al.*, Designing Mechanical Properties of 3D Printed Cookies through Computer Aided Engineering, *Foods*, 2020, **9**(12), 1804.
- 16 H. S. Tan, Y. T. Verbaan and M. Stieger, How will better products improve the sensory-liking and willingness to buy insect-based foods?, *Food Res. Int.*, 2017, **92**, 95–105.
- 17 P. L. Fuhrmann, G. Sala, M. Stieger and E. Scholten, Effect of oil droplet inhomogeneity at different length scales on mechanical and sensory properties of emulsion-filled gels: length scale matters, *Food Hydrocolloids*, 2020, 101.
- 18 M. Santagiuliana, M. Christaki, B. Piqueras-Fiszman, E. Scholten and M. Stieger, Effect of mechanical contrast on sensory perception of heterogeneous liquid and semi-solid foods, *Food Hydrocolloids*, 2018, **83**, 202–212.
- 19 J. I. Lipton, M. Cutler, F. Nigl, D. Cohen and H. Lipson, Additive manufacturing for the food industry, *Trends Food Sci. Technol.*, 2015, **43**(1), 114–123.
- 20 P. J. Lillford, The Importance of Food Microstructure in Fracture Physics and Texture Perception, *J. Texture Studies*, 2011, **42**(2), 130–136.
- 21 L. Wasserman, *All of Statistics: A Concise Course in Statistical Inference*. Springer, 2010.
- 22 M. Zampini and C. Spence, Assessing the Role of Sound in the Perception of Food and Drink, *Chemosens. Percept.*, 2010, **3**(1), 57–67.
- 23 R. G. Munro and S. W. Freiman, Correlation of Fracture Toughness and Strength, *J. Am. Ceram. Soc.*, 2004, **82**(8), 2246–2248.
- 24 L. Hao, S. Mellor, O. Seaman, J. Henderson, N. Sewell and M. Sloan, Material characterisation and process development for chocolate additive layer manufacturing, *Virtual Phys. Prototyping*, 2010, **5**(2), 57–64.
- 25 S. Beckett, *The Science of Chocolate*. The Royal Society of Chemistry, 2008.
- 26 H. Schenk and R. Peschar, Understanding the structure of chocolate, *Radiation Phys. Chem.*, 2004, **71**(3), 829–835. 9th International Symposium on Radiation Physics (ISRP-9).
- 27 S. Zhu, M. Ribberink, M. de Wit, M. Schutyser and M. Stieger, Modifying sensory perception of chocolate coated rice waffles through bite-to-bite contrast: an application case study using 3D inkjet printing, *Food Funct.*, 2020, **11**, 10580–10587.
- 28 M. P. Bendsøe and N. Kikuchi, Generating optimal topologies in structural design using a homogenization method, *Comput. Methods Appl. Mech. Eng.*, 1988, **71**(2), 197–224.
- 29 O. Sigmund, *Design of material structures using topology optimization*. Department of Solid Mechanics, Technical University of Denmark, 1994.
- 30 J. Zhang, F. van Keulen and A. M. Aragón, On tailoring fracture resistance of brittle structures: A level set interface-enriched topology optimization, *Comput. Methods Appl. Mech. Eng.*, 2022, **388**, 114189.
- 31 M. Silva, P. H. Geubelle and D. A. Tortorelli, Energy release rate approximation for small surface-breaking cracks using the topological derivative, *J. Mech. Phys. Solids*, 2011, **59**(5), 925–939.
- 32 Z. Kang, L. Pai and M. Li, Topology optimization considering fracture mechanics behaviors at specified locations, *Structural and Multidisciplinary Optimization*, 2017, **55**(5), 1847–1864.
- 33 J. Hu, S. Yao, N. Gan, Y. Xiong and X. Chen, Fracture strength topology optimization of structural specific position using a bi-directional evolutionary structural optimization method, *Eng. Optimization*, 2019, 583, DOI: 10.1080/0305215X.2019.1609466.
- 34 S. J. van den Boom, J. Zhang, F. van Keulen and A. M. Aragón, An interface-enriched generalized finite element method for level set-based topology optimization, *Structural and Multidisciplinary Optimization*, 2021, **63**(1), 1–20.
- 35 M. Beghini, L. Bertini and V. Fontanari, Stress intensity factors for an inclined edge crack in a semiplane, *Eng. Fract. Mech.*, 1999, **62**(6), 607–613.

